14. PHOTOMETRIC TREATMENT

The Hipparcos main catalogue includes information related to the stellar magnitudes as derived from the photon counts recorded by the main detector (the image dissector tube) and the star mapper detectors (B_T and V_T). This chapter provides an overview of the treatment of the photometric data obtained from the reduced image dissector tube photon counts. It describes briefly the processing of the raw photon counts, the definition of the Hipparcos photometric system, the photometric reduction models and techniques used by the two consortia, and finally the results obtained in the comparisons of the final consortia results and their merging to produce the Epoch Photometry Annex and Extension. The photometry obtained from the star mapper detectors is described in Chapter 6 and in Volume 4.

14.1. Introduction

The Hipparcos mission was designed to carry out high precision astrometric measurements for some 118 000 pre-selected stars. During the preparation for the mission it became clear that the on-board detectors (the image dissector tube, and the star mapper detectors) could also be employed to analyse and monitor the intensity of the starlight. The magnitudes obtained for each programme star with the main detector would be of relatively high precision, defined in an all-sky uniform wide-band filter, referred to as *Hp*.

The main detector was positioned behind a modulating grid in the focal plane of the instrument. It registered the transits of selected objects through photon counts over 1/1200 s intervals. The photon counts reflected the stellar intensity, modulated by the grid. The reduction of these photon counts to a simple modulated signal is described in Chapter 5. The result of this reduction was a signal that represented the estimated values of the observed counts N_k as:

$$\mathrm{E}[N_k] \equiv I_k = I_b + I_s\left(1 + M_1 \cos g_1 + M_2 \cos(2g_1 + 2g_2)\right) \qquad [14.1]$$

where I_s represents the intensity of the object, I_b the background intensity, g_1 and $g_1 + g_2$ the phase of the first and second harmonics, and M_1 and M_2 the modulation coefficients of the first and second harmonics. Two measurements for the intensity of the object could be derived from Equation 14.1: the zero level or dc component, given by $I_s + I_b$ and the amplitude of the first harmonic or ac component, given by $I_s M_1$ (NDAC) or a weighted average of $I_s M_1$ and $I_s M_2$ (FAST). Both I_s and $M_{1,2}$ were functions of the position in the field of view and of the colour of the object. These relations, in addition,

changed as a function of time. In order to use the dc component, it was necessary to define and subtract the background contribution I_b. The aim of the photometric calibrations was to describe these corrections and to derive from the observed dc and ac components of Equation 14.1 the best estimates of the magnitude Hp:

$$Hp = 2.5 \log \tilde{I}_s + \text{constant} \qquad [14.2]$$

Equation 14.1 was always solved for data accumulated over an interval of 32/15 s, referred to as a frame transit. It took a star 9 to 10 of these intervals to cross the field of view, a duration referred to as a field transit. The photometric reductions were carried out using the frame transits, but for the final data those frame transits belonging to the same field transit were combined to provide one measurement of the stellar magnitude. A total of 13 million such magnitudes were obtained, an average of 110 per star. The typical accuracy was 0.01 mag for an 8 mag star. Data were rather unevenly distributed over the 37 months of the mission, and large variations occur in the number of measurements available (up to 385, depending mainly on ecliptic latitude). The final data, made available as the Hipparcos Epoch Photometry Annex plus Extension, represent the largest homogeneous multi-epoch all-sky photometric survey to date.

The photometric data were initially reduced using photometric standard stars selected on the basis of pre-launch ground-based information, transformed to the pre-launch estimate of the passband Hp. This set of standard stars was updated during the mission to incorporate new stars and reject objects found variable on the basis of the Hipparcos measurements. The new standards were recalibrated to provide an improved representation of the Hp passband. All data were re-reduced using 22 000 standard stars, covering a colour range $-0.3 < V - I < 1.8$ with a pronounced peak in the distribution for $V - I = 0.6$ and two smaller peaks at $V - I = 0.0$ and $V - I = 1.0$. The $V - I$ index used here is the Cousins' colour index, also referred to as $(V - I)_C$ below.

14.2. The Photometric System

The Hipparcos passband corresponded primarily to the spectral response of a S20 photocathode combined with the transmission of the optics. A pre-launch definition was used to predict an Hp value for each programme star from the existing magnitudes and colours. After the first in-orbit calibration a revised definition was obtained and used to produce predicted Hp values for the final set of standard stars, with a precision better than 0.01 mag. This was sufficient to define the magnitude scale with a precision of 0.001 mag twice a day. The Hp band is shown in Figure 14.1, as a function of the wavelength, superimposed on some commonly used broad-band filters. One should note the marked extension of the sensitivity toward the extreme red. The numerical values for the passband are given in Section 1.3 of Volume 1.

The V_J band has more or less the same effective wavelength as Hp, so that the amplitude of $Hp - V_J$ is smaller than 0.2 mag for stars with $(B - V)_J < 1.5$. Several transformation laws were derived to link the Hipparcos photometric systems to the V_J system according to star colours. The difference $Hp - V_J$ as a function of $(V - I)_C$ was very well defined in the range $-0.4 < (V - I)_C < 3.0$, from classical photometry, with uncertainties less than 0.01 mag. The extension to redder stars was obtained from dedicated observations of a set of Mirae with a CCD chain equipped with the Cousins' I band and Johnson-Geneva V band. Thus the transformation was extended up to $(V - I)_C = 5.4$ with an uncertainty

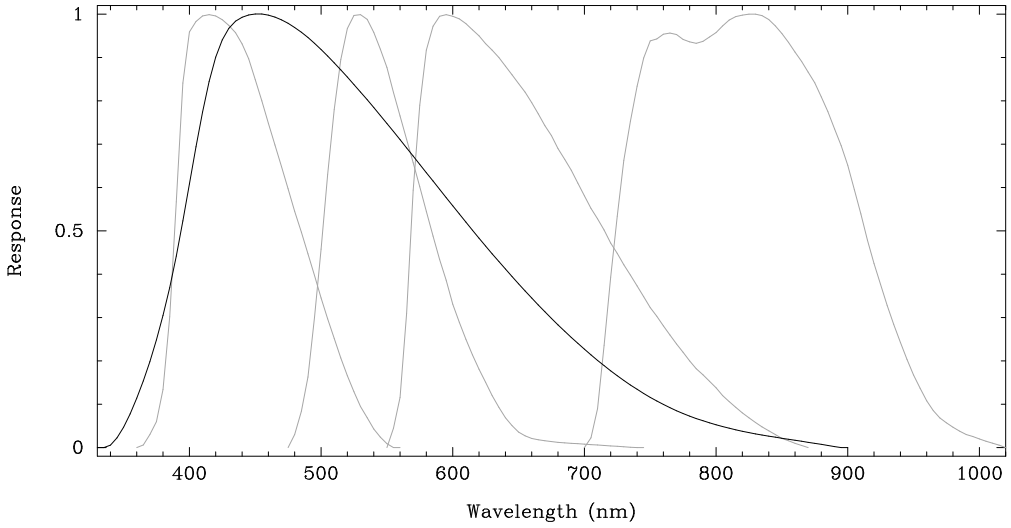

Figure 14.1. *Normalized response curve for the Hipparcos Hp passband (solid line), superimposed on (from left to right) the Johnson B_J, V_J and Cousins' R and I passbands.*

Table 14.1. Relationship between $(Hp - V_J)$ and $(V - I)_C$ for types O to G5, class V to II and red giants of types G5III to M8III.

$V-I$	$Hp-V$	$V-I$	$Hp-V$	$V-I$	$Hp-V$	$V-I$	$Hp-V$
−.50	−.182	.40	.082	1.30	.147	2.90	−0.065
−.45	−.164	.45	.089	1.35	.147	3.00	−0.090
−.40	−.145	.50	.097	1.40	.140	3.20	−0.155
−.35	−.126	.55	.106	1.45	.135	3.40	−0.235
−.30	−.107	.60	.115	1.50	.128	3.60	−0.325
−.25	−.088	.65	.125	1.60	.116	3.80	−0.425
−.20	−.070	.70	.133	1.70	.106	4.00	−0.535
−.15	−.053	.75	.141	1.80	.096	4.20	−0.65
−.10	−.035	.80	.147	1.90	.090	4.40	−0.76
−.05	−.018	.85	.154	2.00	.082	4.60	−0.87
.00	.002	.90	.159	2.10	.072	4.80	−0.98
.05	.018	.95	.164	2.20	.060	5.00	−1.10
.10	.036	1.00	.167	2.30	.048	5.50	−1.38
.15	.050	1.05	.168	2.40	.032	6.00	−1.66
.20	.061	1.10	.168	2.50	.018	6.50	−1.94
.25	.068	1.15	.165	2.60	.001	7.00	−2.22
.30	.072	1.20	.162	2.70	−.018	8.00	−2.78
.35	.076	1.25	.157	2.80	−.040	9.00	−3.34

Table 14.2. Relationship between $(Hp - V_J)$ and $(V - I)_C$ for G, K, M dwarfs with $(V - I)c > 0.70$.

$V-I$	$Hp-V$	$V-I$	$Hp-V$	$V-I$	$Hp-V$	$V-I$	$Hp-V$
0.70	.133	1.10	.138	1.50	.108	2.20	.050
0.75	.137	1.15	.133	1.55	.105	2.30	.041
0.80	.140	1.20	.129	1.60	.102	2.40	.034
0.85	.142	1.25	.125	1.70	.093	2.50	.022
0.90	.144	1.30	.122	1.80	.085	2.60	.001
0.95	.146	1.35	.119	1.90	.076	2.70	-.023
1.00	.145	1.40	.115	2.00	.066		
1.05	.142	1.45	.112	2.10	.058		

Table 14.3. Relationship between $(V - I)_C$ and $(B - V)_J$ for early type stars and red giants.

$V-I$	$B-V$	$V-I$	$B-V$	$V-I$	$B-V$	$V-I$	$B-V$
−0.379	−0.345	0.190	0.174	0.804	0.765	1.334	1.365
−0.299	−0.276	0.252	0.228	0.847	0.825	1.392	1.413
−0.231	−0.216	0.331	0.291	0.897	0.893	1.473	1.464
−0.168	−0.164	0.412	0.351	0.946	0.960	1.567	1.527
−0.105	−0.119	0.482	0.415	0.995	1.021	1.617	1.550
−0.050	−0.072	0.553	0.482	1.050	1.088	1.644	1.568
0.002	−0.020	0.617	0.543	1.107	1.143	1.724	1.583
0.040	0.021	0.667	0.597	1.155	1.196	1.831	1.604
0.072	0.062	0.722	0.659	1.211	1.253	1.882	1.615
0.124	0.110	0.770	0.717	1.271	1.311	2.021	1.635

Table 14.4. Relationship between $(V - I)_C$ and $(B - V)_J$ for K and M dwarfs.

$V-I$	$B-V$	$V-I$	$B-V$	$V-I$	$B-V$	$V-I$	$B-V$
0.631	0.550	1.042	0.999	1.567	1.348	2.725	1.650
0.670	0.601	1.103	1.050	1.645	1.390	2.874	1.700
0.707	0.648	1.175	1.100	1.785	1.445	3.008	1.750
0.747	0.699	1.244	1.149	1.905	1.472	3.144	1.800
0.788	0.749	1.333	1.199	2.054	1.498	3.478	1.900
0.840	0.800	1.386	1.228	2.255	1.524	3.630	1.955
0.893	0.850	1.410	1.250	2.440	1.550	4.100	2.114
0.941	0.898	1.494	1.300	2.544	1.575	4.328	2.198
0.997	0.949	1.535	1.326	2.601	1.600	4.630	2.300

of 0.03 to 0.05 mag. The values up to $(V-I)_C$ = 9.0 resulted from a linear extrapolation and covered the whole range of $(V-I)_C$ colours in the Hipparcos Catalogue.

The final relationships between $(Hp - V_J)$ and $(V-I)_C$ for O, B, A, F, and G<G5 stars with low reddening and for G5 to M8 giants are given in Table 14.1. Table 14.2 gives the relationship for K and M dwarfs. The difference between both relationships is usually less than 0.03 mag and may be disregarded for most of the applications.

For the sake of completeness, it is useful to provide links with photoelectric photometry. The colour index $(V-I)_C$ is related to the Johnson $(V-I)_J$ as follows:

$$\begin{aligned}
(V-I)_J < 0.0 \quad &\Rightarrow \quad (V-I)_C = 0.713\,(V-I)_J \\
0.0 < (V-I)_J < 2.0 \quad &\Rightarrow \quad (V-I)_C = 0.778\,(V-I)_J \\
2.0 < (V-I)_J < 3.0 \quad &\Rightarrow \quad (V-I)_C = 0.835\,(V-I)_J - 0.13
\end{aligned}$$

The relationships between $(V-I)_C$ and $(B-V)_J$ are summarized in Tables 14.3–14.4 for early-type stars and red giants, and for late type stars, respectively.

14.3. The Photometric Data

The Signal

As shown in the introduction, the photometric information obtained from the reduced image dissector tube photon counts consists of a dc component, $I_s + I_b$ and an ac component, $I_s M_1$ (or a weighted combination of $I_s M_1$ and $I_s M_2$), obtained over a frame transit of 32/15 s. For single stars the photometric information was entirely contained in both the ac and dc components, while for multiple stars, there was no such simple separation between the amplitudes of the modulated signal and the photometric information. These stars had to be processed separately (see Chapter 13).

The response I_s for an 8 mag star with $(V-I)_C$ = 0.5 mag, in the centre of the field, dropped from 6600 Hz at the start of the mission to 4000 Hz at the end. With $(V-I)_C$ = 2.5 mag it dropped from 5500 Hz to 4000 Hz. These changes with time were due to the 'ageing' of the optics (see Section 14.5). The background I_b varied between 20 and 70 Hz, except during the crossing of the radiation belts when it reached higher values. As the image of a star crossed the grid over an angular distance of $0^\circ\!.9$ it was observed on average in 9 observational frames. After the calibration was applied to each frame, either (FAST) the median of the 9 frame magnitudes or (NDAC) a weighted mean (with a rejection of outliers) were computed to produce the Hipparcos magnitude of the field transit.

The ultimate precision, if only limited by the photon noise, would be given by:

$$\sigma^2(I_s) = \frac{I_s + I_b}{T} \qquad [14.3]$$

where T is the time, expressed in seconds, allocated to the star during a field transit. This was of the order of 4 seconds on the average, less for brighter stars and more for

fainter ones. T also depended on the number of other stars also competing for observing time. From this expression we can derive:

$$\sigma(Hp) \approx \frac{\sigma(I_s)}{I_s} \approx \frac{1}{\sqrt{I_s\,T}} \qquad [14.4]$$

which led respectively to an internal precision of 0.005, 0.01, 0.02 mag for stars of magnitude 6, 8, 10. While a very careful calibration has allowed this precision for stars fainter than 8 mag to be reached, it was not reached for bright stars because of small systematic effects which remained uncalibrated.

The Two Magnitude Scales

As explained above, the photometric information is contained in both the unmodulated (dc) intensity $I_s + I_b$ and in the modulated (ac) amplitudes $I_s M_{1,2}$. The resulting magnitudes are designated by $Hp_{\rm dc}$ and $Hp_{\rm ac}$. For single stars both magnitudes are identical in expectation. However, the relative error on the estimated amplitude for a sinusoidal signal is $\sqrt{2}$ times larger than the relative error on the mean level. Since the value of the modulation coefficient was $M_1 \approx 0.7$, the absolute errors on the ac components were on average twice those on the dc components.

The two magnitudes were calculated at every field transit and appear, together with their standard deviation, in the Hipparcos Epoch Photometry Annex (HEPA) and the Hipparcos Epoch Photometry Annex Extension (HEPAE). Strictly, only $Hp_{\rm dc}$ should be used as a realization of the Hp scale. A comparison between $Hp_{\rm ac}$ and $Hp_{\rm dc}$ can be used to test the hypothesis that the object observed is a single point source. Any deviation from this assumption, such as duplicity or extension, will show up from a comparison of the two magnitudes. Occasionally, an accidental duplicity arose when a parasitic star from the complementary field of view was mapped on the focal plane near to the programme star. In this case, $Hp_{\rm dc}$ appears brighter than the observations made in the other field of view (where the same superposition could not take place) and, at the same time, $Hp_{\rm ac}$ becomes fainter than $Hp_{\rm dc}$ (i.e. $Hp_{\rm ac} > Hp_{\rm dc}$).

The ageing corrections (see Section 14.5) applied to the ac magnitudes were less rigorously determined than the corrections for the dc magnitudes. Detailed comparisons between ac and dc magnitudes are meaningless for very red stars, as their ac magnitudes can still contain small uncorrected, colour related systematic errors.

The Timescale

In the Hipparcos Epoch Photometry Annex all the field transits of each star are listed in chronological order of barycentric Julian days: BJD − 2 440 000. This timescale is based on Terrestrial Time (TT) as explained in the general introduction to the Hipparcos Catalogue. Times were corrected to the barycentre using the barycentric Earth ephemeris (Section 12.1) to correct for light-time effects. The epoch $t_{\rm E}$ of arrival of the starlight on Earth was transformed into $t_{\rm B}$ for the arrival at the solar system barycentre by:

$$t_{\rm B} - t_{\rm E} = \mathbf{b}'_{\rm E}\mathbf{u}c^{-1} \qquad [14.5]$$

where $\mathbf{b}_{\rm E}$ is the barycentre–Earth vector, $\mathbf{u}$ the unit vector in the direction of the star, and c the speed of light. This well known correction had a range between −5.6 and +5.6 minutes (limited by the constraints of the scanning law) and was evaluated for every field transit.

14.4. The Calibration

The Principles

The intensities I_s+I_b and I_sM_1, I_sM_2 recorded at each observational frame were affected by instrumental effects, which had to be taken into account in order to obtain the stellar magnitude. The following effects were calibrated and removed:

(1) the inhomogeneity of the sensitive surface and of the residual defects of the optics made the sensitivity of the detector variable over the field of view. This was represented mathematically in various ways;

(2) the ageing of the optics and of the detector caused a steady decrease in the overall sensitivity, with a marked chromatic dependence. The ageing was more pronounced in the blue than in the red. This was represented by the colour-terms in the calibrations;

(3) the sensitivity was not exactly the same in the preceding and following field of view. Solutions had to be made separately for the two fields of view.

In addition to these instrumental effects, the background contribution had to be calibrated and removed from the dc component. A calibration programme aimed at converting the observed intensity at each observational frame into Hp was run on all data collected during an orbital period. Due to a 1 to 3 hour interruption of the observations during the perigee passage, the orbital period became a useful unit for calibrations and definition of data sets. The same unit was also used to constrain the data used in the great-circle reductions.

Only measurements of standard stars were used in the calibration. These measurements were still subjected to a series of quality tests, in order to reduce the number of faulty data-points. A linear model, describing generally small corrections to an underlying model, was used to fit the data, using a standard least-squares procedure.

Two different methods were used by the FAST and NDAC consortia in processing the photometric data. In FAST the fits were done by adjusting the computed intensity of the standard stars to the observed intensity, while NDAC fitted their model in magnitude scale. The variables used in the models were somewhat similar, but the techniques employed were different enough to justify a separate presentation of the FAST and NDAC procedures.

The Basic Model Used by FAST

Let $\tilde{I} = I_s + I_b$ be the observed mean intensity on a particular observational frame of a standard star and $I_{\rm ref}$ the computed intensity derived from its *a priori* magnitude. With $(1-\epsilon(G,H,C))$ representing the *a priori* model correction of the intensities as a function

of colour (C) and position in the field (G, H), the functional relationship between these quantities was given by:

$$\tilde{I}(1-\epsilon) = I_{\rm ref} \sum_{k=1}^{13} a_k X_k + b_0 + b_1 f_1(\lambda - \lambda_\odot, \beta) + b_2 f_2(b) \qquad [14.6]$$

where the X_k are listed in Table 14.5. The determination of the colour terms was given great attention because of their importance in defining the photometric system. The set of standard stars was sparse for stars redder than 1.5 mag, although the calibration had to be applied to many late-type stars included in the Hipparcos programme. In the FAST solution, to limit the risk of extrapolating the calibration formulae outside the range of validity, additional calibration red stars were included. This was done by adding single stars brighter than $Hp = 9.5$ mag and with colours in the range 1.6 mag < $V - I$ < 2.2 mag, provided the *a priori* standard deviation in magnitude was less than 0.009 mag and $\sigma_{V-I} < 0.05$ mag. This was sufficient to constraint the quadratic terms up to $V - I = 2.2$ mag. Then, in the application of the formula, the extrapolation was limited to the linear term above this colour and up to $V - I = 3$ mag, preserving the continuity at each boundary.

The final three coefficients in Equation 14.6 represent the modelling of the unmodulated light, where λ, β are the ecliptic longitude and latitude of the star, $\lambda_\odot$ the ecliptic longitude of the Sun and b the galactic latitude of the star. These three terms were present for the calibration of $Hp_{\rm dc}$ but obviously not for that of $Hp_{\rm ac}$. Each calibration spanned an orbital period (a theoretical maximum of 10 hours but in practice 6 to 8 hours of data, referred to as a data set).

The coefficients (three for each field of view) were kept constant within a data set, which means that the mean background was likely to be underestimated during the crossing of the van Allen belts at either end of an orbit. The information for these coefficients was mainly derived from observations of faint stars. Extra faint stars were added to those originally included in the set of standard stars, in such a way that they did not directly influence the other coefficients. The stars added were single stars fainter than $Hp = 10.7$ mag and with $\sigma_{Hp} < 0.007$, $V - I < 2$ mag, $\sigma_{V-I} < 0.1$. Because of the structure of the observation equations this proved to be a very efficient method for determining the background terms without affecting the other terms.

The unmodulated background in the Hipparcos photometry had a typical strength ranging from 20 to 70 Hz, corresponding to a correction of 0.03 to 0.10 mag for a star of 10 mag. It was not constant over the sky and originated primarily from the following sources:

- the detector thermal noise which gave roughly a count level of 20 Hz even when no star was in the instantaneous field of view;
- the zodiacal light brought about by the diffusion of the sunlight by interplanetary dust which exhibited a strong dependence on $\lambda - \lambda_\odot$;
- the scattered faint stars produced an unmodulated count as soon as there were more than one star in the immediate vicinity (< 30 arcsec) of the programme star, irrespective of whether the perturbing objects belonged, or did not belong, to the same viewing direction as the programme star. This effect was at a maximum when one field of view was in the galactic plane and dropped off sharply with galactic latitude;
- radiation associated with the van Allen radiation belts.

In FAST a model for the starlight based on the mean number of stars fainter than $V = 12$ mag as a function of the galactic latitude was considered and fitted to an analytical function $\Phi(b)$ which represented fairly well the normalized galactic luminosity profile, with $\Phi(b) = 1/[1 + 5.3\,(\sin b + \sin^2 b)]$.

The actual model made use of a function $\tilde{\Phi}(b)$ that averaged out to zero over a great circle and at any time the contribution of the preceding and the following field of view were added up, so that:

$$f_2(b) = \tilde{\Phi}(b_p(b)) + \tilde{\Phi}(b_f(b)) \qquad [14.7]$$

where b_p and b_f were respectively the galactic latitude of the preceding and following field of view.

The contribution of the zodiacal light was taken from published mappings and given a tractable analytical representation as:

$$f_1(\lambda - \lambda_\odot,\, \beta) = \frac{1}{[1 - \cos(\lambda - \lambda_\odot)\cos\beta]}\,\frac{1}{[1 + \{1 + [1 + \cos(\lambda - \lambda_\odot)]^2\}|\sin\beta|]} \qquad [14.8]$$

and was computed for the two fields of view. The three coefficients b_0, b_1 and b_2 of Equation 14.6 were derived as explained above for each data set, and used to compute the background contribution for each observation, using Equations 14.7 and 14.8. For an individual star, these values were essentially constant over a field transit. The background determined in this manner was then removed from the raw data. Its value appears in the Hipparcos Epoch Photometry Annex Extension together with the value used by NDAC, so that anomalous deviations of the magnitude that might originate from the background can be traced back.

The *a priori* model $\epsilon(G, H, C)$ took into account the spatial frequency of the sensitivity of the detector in the form of three fixed two-dimensional maps that were established from a large amount of data covering several weeks of observations. Each map was appropriate for a specific colour range and had a resolution of $0\overset{\circ}{.}02$ in each direction. Thus the calibration described by the model above was in fact differential, as most of the spatial variation was accounted for by the maps.

The Basic Model Used by NDAC

In NDAC the model used was not fundamentally different from that of FAST except for the background modelling, which incorporated data acquired with the star mapper. The mathematical expression (see Equation 14.6 for FAST) was given by:

$$-2.5\log_{10}(\tilde{I} - I'_b) - Hp = \sum_{k=1}^{15} a_k\, Y_k \qquad [14.9]$$

where Hp is the calibration magnitude of the standard and the meanings of Y_k are listed in Table 14.6. The colour coefficients were applied without restrictions to stars of all colours. This was known to be wrong for very red stars, but simplest to correct *a posteriori* after the full calibration of the passband had been obtained (see Section 14.5). I'_b was the modelled *a priori* background described below.

The calibrations were carried out in magnitude space. Since the accuracies of the counts were so high (generally better than 10 per cent), this procedure did not cause any bias larger than 0.001 mag in the frame transit magnitudes. Performing the calibrations in magnitude space avoided a large range of values entering the least-squares solution.

Table 14.5. Instrumental parameters for the photometric calibration of FAST.

Parameter k	Variable X_k	Meaning
1	1	Zero point
2	G	Grid abscissa
3	H	Grid ordinate
4	$G \times H$	
5	$P_2(G)$	2nd Legendre polynomial in G
6	$P_2(H)$	2nd Legendre polynomial in H
7	$P_4(G)$	4th Legendre polynomial in G
8	$P_4(H)$	4th Legendre polynomial in H
9	$P_2(G) \cdot P_2(H)$	
10	$C = V - I - 0.65$	Colour
11	$P_2(C)$	
12	$C \cdot G$	mixed term
13	$C \cdot H$	mixed term

Table 14.6. Instrumental parameters for the photometric calibration of NDAC.

Parameter k	Variable Y_k	Meaning
1	1	Zero point
2	$C = V - I - 0.5$	Colour
3	C^2	
4	C^3	
5	G	Grid abscissa
6	H	Grid ordinate
7	$C \cdot G$	Mixed term
8	$C \cdot H$	Mixed term
9	$10^{0.4(Hp-8)}$	Background term
10	R_2	Radial terms
11	R_3	
12	R_4	
13	R_5	
14	R_6	
15	R_7	

Table 14.7. Positions of the reference points of the NDAC radial model in grid coordinate units.

Radial distance	0.0	0.1	0.3	0.5	0.7	0.9	1.1	1.3
Variable name	R_0	R_1	R_2	R_3	R_4	R_5	R_6	R_7

Also, since most of the influences on the intensities act as a factor, when transformed to magnitudes they become offsets, which are generally easier to reconstruct.

While no significant bias was present in the frame transit magnitudes, a small bias of order 0.01 mag was found to be present in the calibrations due to the weighting scheme that had to be used. The size of this bias was determined by Monte Carlo simulation and a correction was applied.

Two features of this model require further explanation: the radial grid dependence and the background model, I'_b.

The model chosen for the calibration of the grid dependence was a radial one, using linear interpolation, in which each observation equation contains terms representing the relative fractions of the two nearest radial reference points. The positions of the reference points in grid coordinate units are given in Table 14.7. It was based on an examination of residuals accumulated as a function of position in the field of view and colour, using several weeks of data.

The central location for the radial dependence was determined to be (0.03, 0.11) in grid coordinate units. This was then considered to be the origin for all radial measurements. The consistency of the central location was confirmed by analysis of maps of residuals as a function of time.

Although the model contained R_0 and R_1 points, they were not solved but set to zero. The reasons for this were that R_0 was effectively the zero point Y_1, and a zero derivative at $R = 0$ was required which implied that R_1 had to be equal to R_0. Points outside $R = 1.3$ were calculated as an extension of the line between 1.1 and 1.3. Thus, this radial model contributed 6 parameters to the overall calibration model.

The variation of the background as a function of time was fairly complicated. Since it generally only affected stars fainter than $Hp \simeq 9$ mag the calibration of it for each transit was difficult due to the relatively small number of standard stars that were affected. In the NDAC solution, only the offset term of the background model (Y_9 in Table 14.6) was solved for. The remaining three parts of the model were calculated from the star mapper background count and the positions on the sky of the two fields of view of the satellite. The three contributions to the background accounted for in the NDAC model were:

(1) van Allen radiation belts (maximum 100 Hz);

(2) zodiacal light (peak 30 Hz);

(3) the Milky Way (peak 20 Hz).

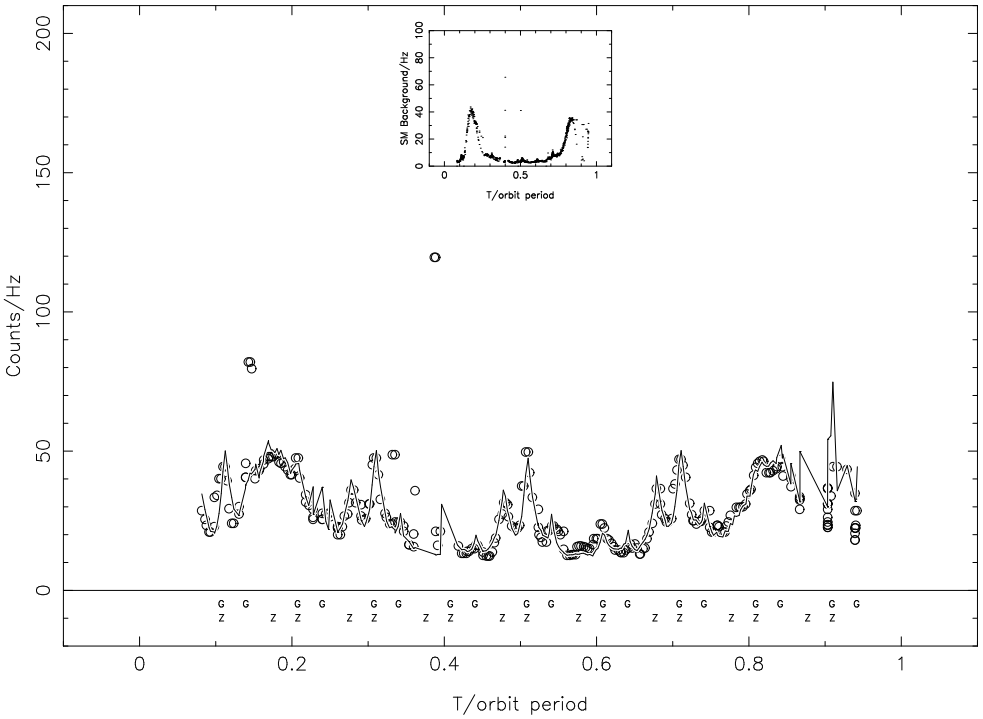

Figure 14.2. *An example of a stretch of data with poor satellite pointing. The data points show the value of the background as measured by the satellite and the line shows the independently derived NDAC background model. All three components of the model are noticeable in this diagram. The position of the Zodiacal light and Milky Way contributions are indicated respectively by the letters Z and G at the bottom of the diagram. The van Allen radiation belt contribution can be seen by comparison with the star mapper background shown in the inset diagram (the units are the same as for the main diagram).*

The parameters used in this part of the model were derived mainly from stretches of data with poor satellite pointing so that the background was being sampled rather than the target stars. An example of such a stretch of data is given in Figure 14.2.

The largest contribution was caused by radiation associated with the van Allen radiation belts and was very variable from orbit to orbit. It mainly affected data at the start and end of a data set. Using data such as in Figure 14.2, a correlation was found between the radiation-induced star mapper background and the main mission background. The star mapper background was measured regularly, which allowed the radiation contribution to the image dissector tube background to be determined. If this background contribution was larger than approximately 100 Hz the frame transit was rejected.

While the contributions of zodiacal light and the Milky Way were noticeable in the star mapper data too, they did not scale in the same way as the radiation contribution. It was thus necessary to assume that these were approximately constant over time and just functions of sky position. The forms adopted were derived mainly from the data and checked against what was expected from the literature.

The form of the Zodiacal light contribution to the background model was given by:

$$30 \text{ Hz} \times \max\left[0.0, \left(1 - \frac{|\beta|}{45^\circ}\right)\right] \times \max\left[0.085, \left(1 - \frac{(|\lambda - \lambda_\odot| - 40^\circ)}{60^\circ}\right)\right] \qquad [14.10]$$

and that for the galactic contribution by:

$$20 \text{ Hz} \times \left|\cos\frac{l}{2}\right| \times \frac{1}{1 + (2|b|/15^\circ)} \qquad [14.11]$$

where (λ, β) and (l, b) are the ecliptic and galactic coordinates respectively of the centres of the field of view. Values were calculated for both the preceding and following fields of view.

The value given in the Hipparcos Epoch Photometry Annex Extension for each transit is the combination of all three contributions along with the background offset determined, Y_9.

The calibration to convert the counts to Hp magnitudes was a least-squares solution using the method of Householder transformations (Bierman 1977), with weights applied to the observation equations according to the estimated errors of the observations.

The calibrations were carried out on data accumulated over approximately one orbit (10 hours). Separate solutions were carried out for both the preceding and following fields of view and for both $Hp_{\rm dc}$ and $Hp_{\rm ac}$. The solution was calculated iteratively with an *a posteriori* four sigma filter being applied to the data to reduce the effect of outliers.

The use of the Householder transformations made the application of a running solution between the calibrations particularly easy. The prime advantage of this was to ensure the stability of the calibration and to safeguard against the effect of outliers biasing the calibration coefficients. However, this also meant that care had to be taken when it was expected that the coefficients could undergo sudden changes. This was likely to occur after a refocusing of the satellite optics or after a long period of satellite inactivity.

When such sudden changes occurred, it was necessary to reinitialize the running solution in some way. After a refocusing, only a partial reinitialization was required since only a few coefficients were affected by this, while after a long period of satellite inactivity a full reinitialization was carried out. Figure 14.3 shows the effect of the reinitializations on M_1, the modulation coefficient of the first harmonic (see Equation 14.1), as derived from the calibration coefficient for the dc and ac components. While most discontinuities were directly related to refocusing of the optics, on one occasion (on day 755, see also Chapter 2, Table 2.1), it was due to restoring proper thermal conditions after a heater failure.

One of the effects not accounted for in the calibrations was the effect of depointing. Inaccurate satellite pointing caused the instantaneous field of view not to be positioned exactly on the target star. This would cause a small attenuation in the intensity of the star. A study was carried out on the consequence of not carrying out a correction for this effect and it was shown that it would only add an additional 0.0006 mag scatter to a field transit.

The calibrations were applied to each frame transit and these were then combined to form a field transit. For stars of extreme colour (redder than $V - I \simeq 2.0$ mag) the calibration had to be extrapolated due to the low number of calibrating standard stars

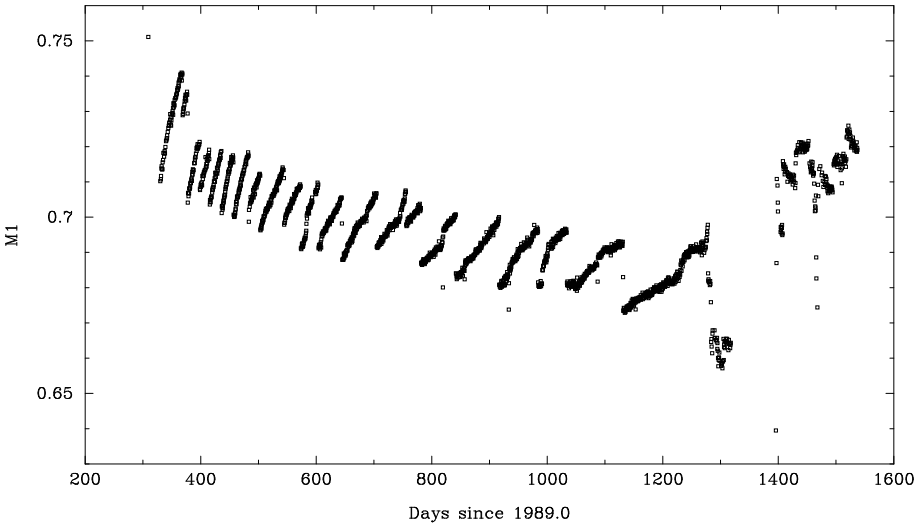

Figure 14.3. *The effect of the reinitializations on the modulation coefficient of the first harmonic in the preceding field of view. The general zig-zag pattern is caused by the partial reinitializations carried out after each refocusing. The jump occurring at day 1400 was due to a full reinitialization carried out after the loss of the gyros. This plot is for a colour of* $V - I = 0.5$ *mag.*

available at these colours. The errors caused by the instabilities inherent in this procedure were later removed during the ageing corrections described in the next section.

The combination of the frame transits to form a field transit was carried out in intensity space. By doing this, biases that might arise from the conversion from intensities to magnitudes were minimized. Also at this stage, outlying frame transits within a field transit were rejected at the 3σ level. If insufficient transits remained, the entire field transit was rejected. Between 1 and 2 per cent of the data was rejected in this manner. The average that was formed out of the remaining transits was a weighted mean since the accuracy of a frame transit varied according to the observing time allocated to it.

14.5. Final Corrections

This section describes corrections applied to the reduced data. These corrections came from three sources:

(1) zero-point shifts;

(2) passband definition, and ageing correction;

(3) final field distortion corrections.

These corrections, although different in detail, were applied to both the FAST and NDAC reduced data after all reductions were completed. All three were derived using the accumulated results from the reductions.

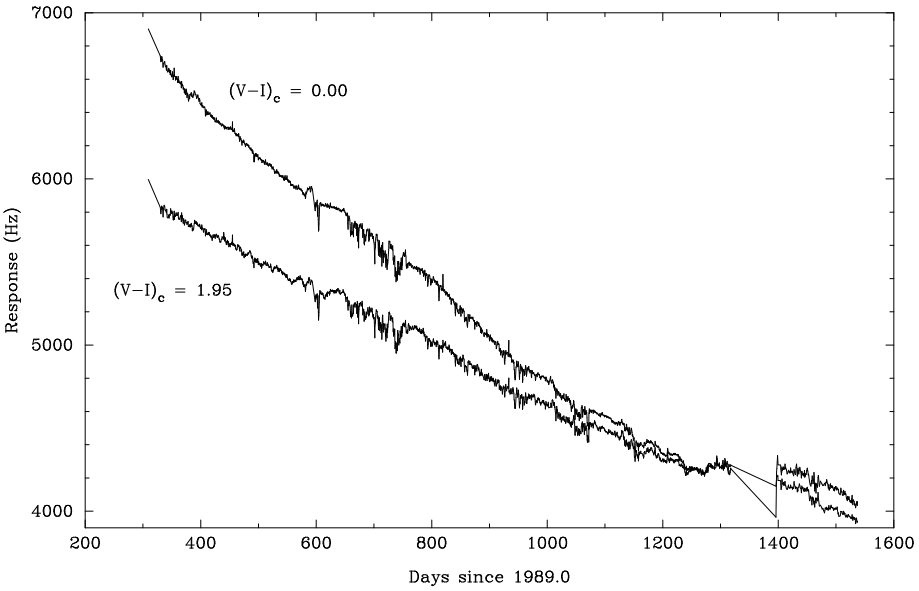

Figure 14.4. *Time variation of the response in the centre of the field for 8 mag stars of two different colour indices, showing the effect of the ageing of the detector chain through the decrease in response over the mission and the difference in this decrease for stars of different colour.*

Zero-point Corrections

After the calibrations had been completed, various checks were carried out on the validity of the photometry. It soon became apparent that the zero points (X_1 and Y_1) were varying by around ±0.01 mag within an orbit. Further investigation showed that these shifts were present in the data of both consortia and that they were not a function of the field of view. Various explanations were considered and investigated, but all were rejected. Neither solar activity nor attitude determination problems matched the pattern of shifts. The temperature of the satellite did not correlate with this effect either. Problems relating to the Milky Way or bright stars were thought unlikely since they would have caused a recurring pattern which was not seen.

The overall effect of these shifts on the mission was equivalent to an additional scatter of 0.003 mag to all transits. Even though the cause of these shifts was not known, it was felt that they had to be corrected. These corrections were applied independently by FAST and NDAC as small magnitude offsets. No investigation (nor correction) was carried out on shifts in the ac component calibrations due to the noisier nature of the data.

Ageing Corrections

The main detector chain contained a large number of optical elements which were affected by radiation during the mission. The radiation resulted in chemical changes in the optical elements, leading to loss of transmission. This transmission loss was most noticeable on the blue wing of the transmission curve, as can be seen from Figure 14.4, which shows the response at the centre of the field of view for stars of different colour over the length of the mission.

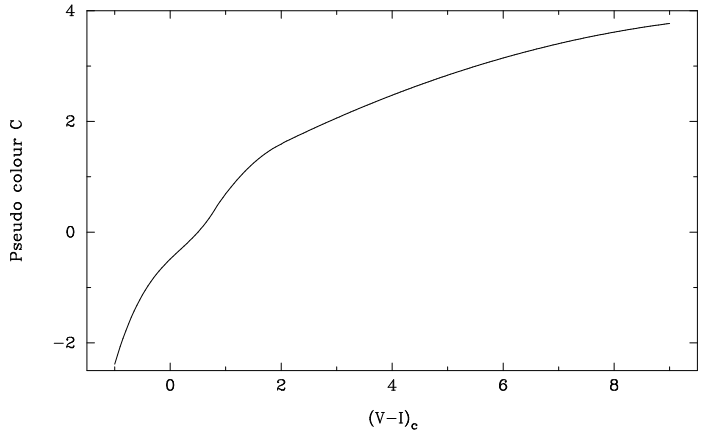

Figure 14.5. *The pseudo-colour C as a function of* $(V-I)_C$.

Table 14.8. Definition of the pseudo-colour index $C = a + b(V-I) + c(V-I)^2 + d(V-I)^3$ for different intervals of $V-I$.

Interval	a	b	c	d
$V-I \leq 0.85$	−0.48729	0.98554	−0.31968	0.592
$0.85 < V-I \leq 2.00$	−1.03936	2.14720	−0.416	0.0
$V-I > 2.0$	0.5152 n	0.592	−0.0256	0.0

The changing passband response was provisionally accommodated through introducing a $(V-I)_C$ dependence in the photometric reductions (as described in the preceding section). However, the coverage in $(V-I)_C$ by the standard stars was insufficient to describe the colour relations for very red ($(V-I)_C > 2.0$ mag) stars. In addition, most stars with very red colours tend to be variable. The *a posteriori* calibration of the *Hp* passband was described in Section 14.2. Using this calibration together with ground-based data on large amplitude red stars (observations by the American Association of Variable Star Observers and specific photoelectric measurements of primarily Mira stars), predicted values for epoch photometry of these red stars were produced. These values were compared with the observed epoch photometry produced by the two consortia, and the observed differences were translated into a new colour correction, which was applied *a posteriori* after removing the old colour correction. This colour correction reduced all the photometric data to the reference passband defined for 1 January 1992.

As a result of the chromatic corrections, the use of a wrong colour for a star in the data analysis shows up in the fully calibrated photometric data as an almost linear drift of the magnitude, with $dHp/dt < 0$ if the true colour is redder than was assumed in the reductions. The epoch photometry can be corrected for such errors. The procedure is as follows. Take the $(V-I)_C$ value used in the data-reductions (Field H75), and transform it into a pseudo-colour C(old) according to the rules described in Table 14.8 and shown in Figure 14.5. Do the same with the improved $(V-I)_C$ index (e.g. as available in Field H40), to obtain C(new). The corrections for the *Hp* magnitudes are then defined as:

$$\delta Hp = Hp(\text{old}) - Hp(\text{new}) = -F(t)\big(C(\text{old}) - C(\text{new})\big) \qquad [14.12]$$

Table 14.9. Definitions of the colour correction factors $F(t)$ expressed as a polynomial in $t - t_0$, for dc and ac magnitudes. t and t_0 are measured in units of 1000 JD, t_0 = 2448.6225 = 1 January 1992.

	dc	dc		ac	
	approx	preceding	following	preceding	following
Stand.dev.	0.0031	0.0012	0.0012	0.0017	0.0017
const	0.0084	0.00303	0.00873	0.0416	0.0478
$(t-t_0)$	−0.0537	−0.04022	−0.04098	−0.0431	−0.0389
$(t-t_0)^2$		0.09000	0.07720	0.1317	0.0338
$(t-t_0)^3$		−0.18863	−0.13772	−0.2384	−0.8277
$(t-t_0)^4$		−0.6746	−0.6735	−1.9387	−2.9383
$(t-t_0)^5$		0.598	0.1322	−2.9443	−3.6662
$(t-t_0)^6$		2.018	2.052	−1.3327	−1.5601
$(t-t_0)^7$		0.340	1.989		
$(t-t_0)^8$		−0.742	0.553		

where $F(t)$ is a function of time and of field of view. Table 14.9 gives approximations to $F(t)$ for dc and ac magnitudes, and the associated standard errors. These standard errors are equivalent to the expected noise on the Hp corrections for a colour correction of 1 mag. Also given is an approximate correction for the dc magnitudes, ignoring the field of view differences, which can be used without the need to access the Hipparcos Epoch Photometry Annex Extension files. As can be seen from Figure 14.5, a correction in $(V-I)_C$ for a blue star will cause a larger correction in the pseudo-colour than a similar correction for a very red star. Information on the field of view can be obtained from the Extension files, where the ac magnitudes are also found. Figure 14.6 shows the observed values of $F(t)$ and the approximating curves. For data obtained beyond day 1300 (JD 2 448 800) it is advised not to use the ac magnitudes for detailed comparisons. The ac magnitudes were sensitive to the focal setting of the telescope, which itself was sensitive to temperature variations. Such variations were quite strong when the telescope was moved to sun-pointing mode, which occurred 3 times after JD 2 448 800.

The data presented in Tables 14.8 and 14.9 also allow in principle for a redefinition of the colour correction in case more accurate data becomes available, but such corrections, if at all justifiable, are expected to be very small.

Field Distortion Corrections

After the calibrations had been carried out an investigation was made into the variations of Hp as a function of the field coordinate H (the direction of the grid slits). A systematic variation with a peak-to-peak variation around 0.008 mag was detected in the NDAC data. Although this would only add an additional scatter of around 0.002 mag to the field transits it was felt that this correction should be made since it was straightforward and would not adversely delay the processing. The corrections made were a function of H, $(V-I)_C$, time and field of view. An example of the size of the correction is given in Figure 14.7. No correction as a function of G, the perpendicular field coordinate, was possible since a field transit consists of an average over a range of G values, i.e. the frame transits. The need for the correction is a consequence of not using a detailed mapping function in the early stages of the calibration. This was confirmed by analysing a residual array that was accumulated as a part of the NDAC diagnostics. By summing

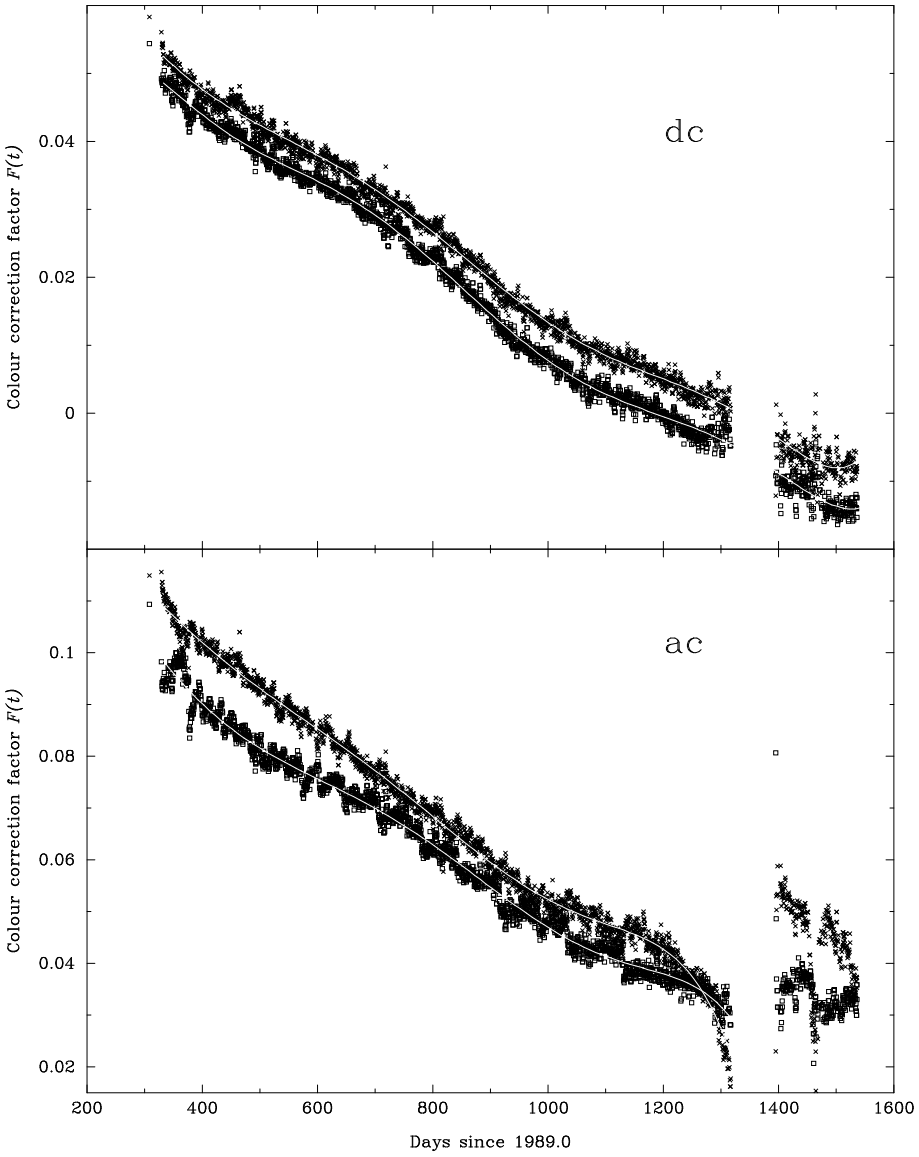

Figure 14.6. *The colour correction factor as derived for the dc (top) and ac magnitudes (bottom). The preceding field of view is indicated with open squares, the following field of view with crosses.*

this array over G a similar correction could be found. This is shown as the dotted line in Figure 14.7. The diagnostic data could not be used directly since it was not detailed enough. Corrections were also carried out to the FAST data, but since some form of mapping function was applied by FAST, the corrections were smaller. No corrections were applied to the ac component.

14.6. Parasitic Transit Detections

Due to the design of the satellite it was possible for a star from the other field of view to be located by chance at almost the same position on the detector as the star being observed. This had the effect of making the star being observed appear brighter. Since

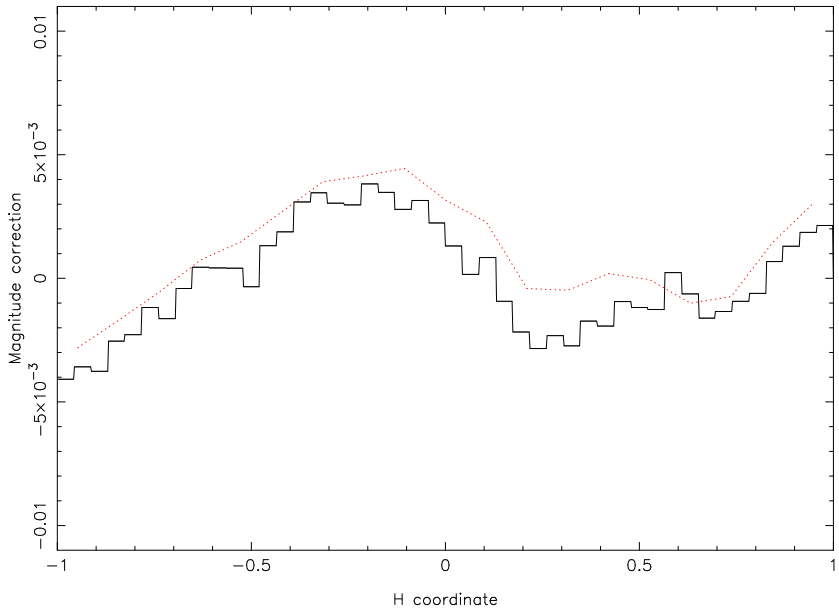

Figure 14.7. *An example of the magnitude corrections applied to the NDAC data as a function of field coordinate, H. This is at mid-mission for the preceding field of view and a star of $V - I = 0.5$ mag. The dotted line shows the correction deduced from the mapping diagnostic for approximately the same parameters.*

this would have had a harmful effect on the variability analysis carried out on the data, it was important that these transits were identified. In order to do this, two methods were employed.

The first method was to search the Tycho Input Catalogue for possible contaminants given an accurate position for the other field of view calculated from the attitude determination. Using this information, along with the attenuation profile of the instantaneous field of view (see Section 5.1), it was possible to determine whether a transit was contaminated. The limit chosen was a perturbation of 0.01 mag. About 100 000 transits were flagged this way. The magnitude and colour (if available) of the contaminating star was retained in the coincidence file of the Hipparcos Epoch Photometry Annex Extension. The position of the other field of view for every field transit has also been retained in the Extension so that future checks may be carried out using more complete catalogues.

Since the accurate position of the other field of view was only available to the NDAC photometric calibration process, the FAST-only transits have not had this analysis performed on them. Because of this and the limiting magnitude of the Tycho Input Catalogue being $V = 10.5$ mag, it was felt that some additional checks were required in order to further identify parasitic transits. This was done by investigating the difference between the ac and dc components for each transit. If a star appeared in the other field of view, in addition to making the target star appear brighter, it also caused the star to appear as a double. The limit chosen for this was 3σ. A limitation of this method was that it could only be carried out on stars thought to be single. About 70 000 transits were flagged this way. In the case of FAST, transits contaminated by the presence of programme stars from the complementary field of view were removed at an early stage of the processing.

14.7. Merging

After the corrections described in the previous section had been applied to both the FAST and NDAC photometric data, a final comparison was carried out in order to best determine the merging strategy.

The main comparison was between the median photometric value of the two consortia for each star. Care was taken that the median calculations were carried out on exactly the same set of observations since the two consortia have slightly different coverage. This is most important for the very red stars since they are variable.

As a function of magnitude (in these comparisons only the dc magnitudes were considered) the systematic differences were very small. Brighter than 10 mag the differences were less than 0.001–0.002 mag. Fainter than this, a larger systematic difference was seen, equivalent to a difference in background of under 2 Hz. This comparison is shown in Figure 14.8.

Also shown are the differences as a function of $V - I$. The systematic differences are less than 0.002 mag out to $V - I = 3.0$ mag. Redder than this the differences are probably less than 0.02 mag out to $V - I = 8.0$ mag. There is not much data at this very red end, and saying more about the level of difference would probably not be possible. The low level of systematic differences was expected as a consequence of the way that the ageing corrections had been carried out.

Investigations on the quoted errors of the field transits for both consortia were also carried out. Most of these consisted of detailed Monte Carlo simulations to see if the observed quoted error distribution could be reproduced. The unit weight residuals were also investigated in this analysis. The two main points arising from this work were:

(1) the quoted error was inaccurate and biased due to only having a small number of frame transits per field transit. This is expected to follow a Student's t distribution. A consequence of this is that if left uncorrected, the unit weight residuals will tend to show a large number of spurious variables;

(2) an uncalibrated and unknown residual that affects a field transit's quoted error is present thus giving larger quoted errors than in the Monte Carlo simulations.

The final conclusion was that some form of empirical correction had to be made to the quoted errors: it was known that the quoted errors were biased from (1) and that no theoretical estimate could be made from (2). The correction that was made was a function of magnitude, quoted error and consortium. It should be noted that when the data were merged another error analysis and correction was carried out to accommodate correlations between the FAST and NDAC data.

These error estimate corrections have implications for any micro-variability analysis carried out on the data. After applying such corrections, all that could be stated is that a star is more variable than stars of similar magnitude. For example, if all stars were variable we could not detect them as such since the errors were scaled. It could be argued that the unknown residual mentioned above (2) could be due to stellar variability.

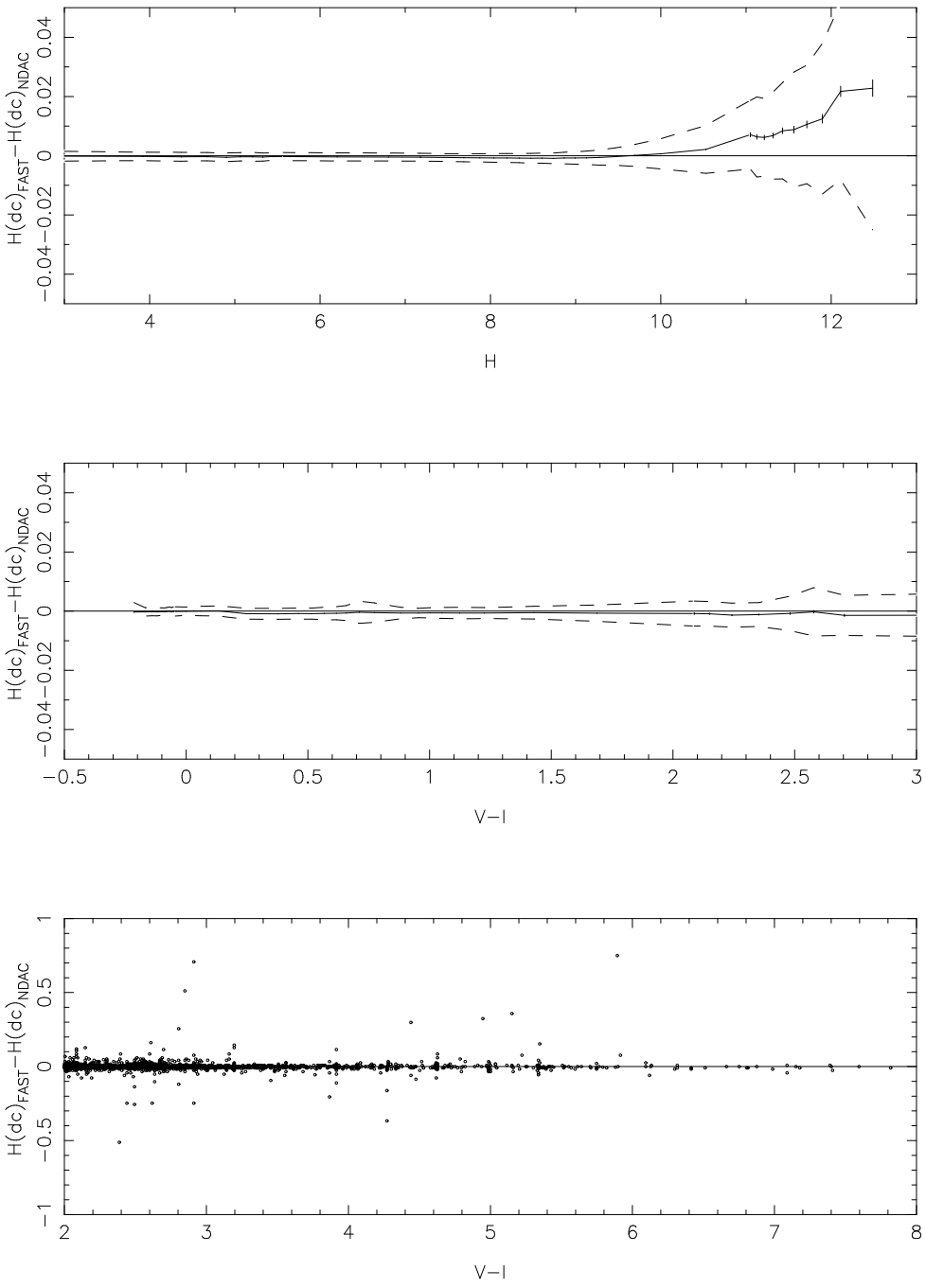

Figure 14.8. *Comparison between FAST and NDAC for $Hp_{\rm dc}$ magnitudes as a function of magnitude and $V-I$. For the top two diagrams the solid line is the median of distribution and dashed line is the 1σ width. The bottom diagram shows the individual data points rather than just the distribution.*

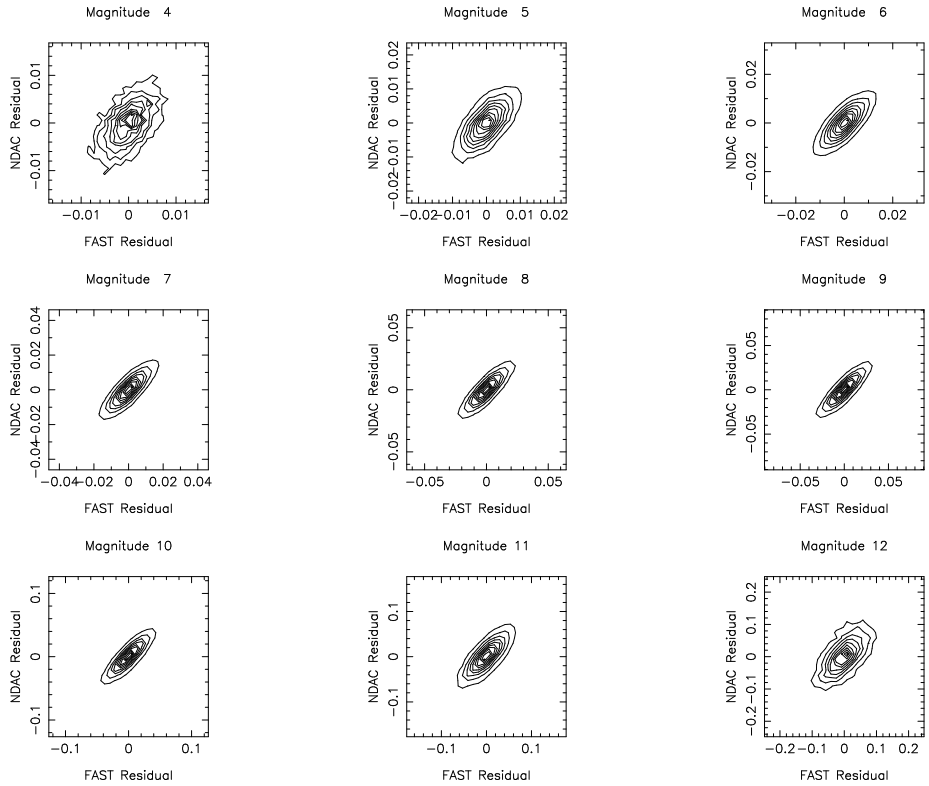

Figure 14.9. *The correlations between FAST and NDAC.*

The level of this would be a few per cent over 20 seconds. It is more likely that this was caused by instrumental effects.

One of the most important things that had to be investigated for the merging process was the level of correlation between the FAST and NDAC data. The results of this investigation are shown in Figure 14.9. These contour plots show the density of the scatterplots of FAST versus NDAC residuals. The residuals are calculated as the differences between each field transit value and the median value for that star and consortium. Only constant stars were used for these investigations.

As is evident from the diagrams, the correlations are very strong. The correlation coefficients range from 0.6 to 0.8, with the highest values for intermediate magnitude stars (7 mag < Hp < 9 mag). This shows that the calibrations agree very well for mid-magnitude stars. Since the same photon counts were used it is expected that any deviation from perfect correlation would occur when the calibrations differ. At the faint end these differences were background related. At the bright end the situation was slightly different and the broadness of the diagrams was caused by the increased sensitivity of the data.

In order to determine how to merge the data an investigation was carried out to see what effect altering the consortia ratio would have on the general scatter of the data. For this investigation a merged magnitude was created using the formula:

$$Hp_{\mathrm{av}} = fHp_{\mathrm{NDAC}} + (1 - f)Hp_{\mathrm{FAST}} \qquad [14.13]$$

The average scatter was then calculated for constant stars. This was then repeated for different fractions (f). The results are shown in Figure 14.10. Since the data were

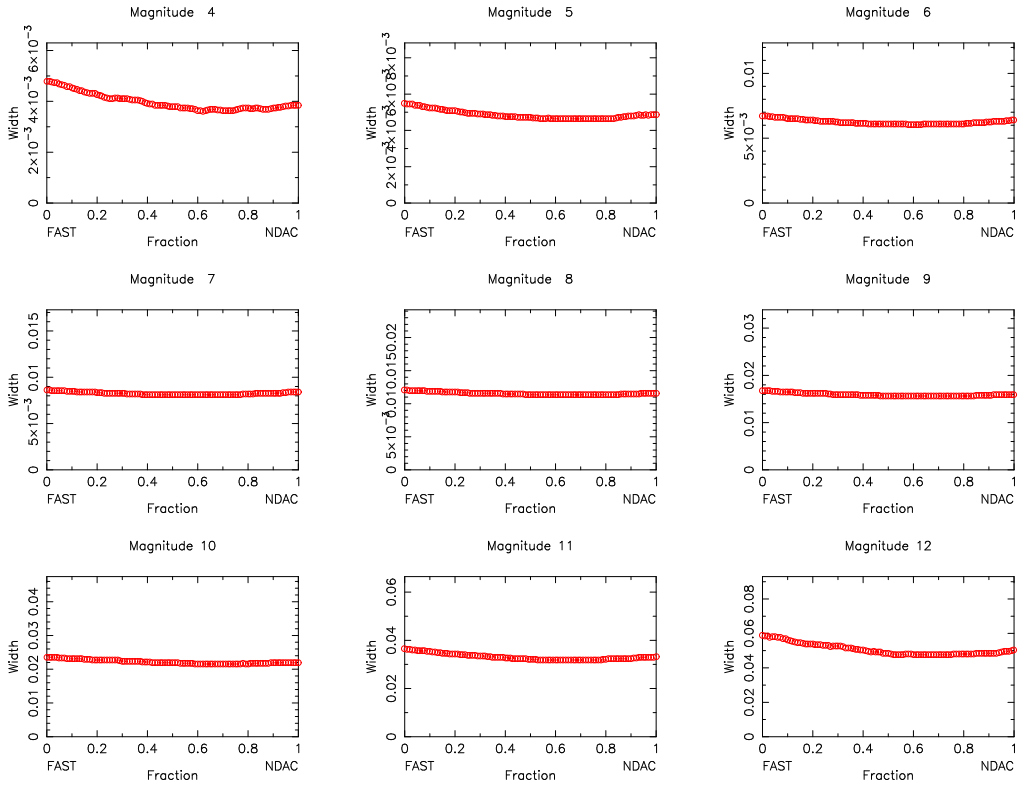

Figure 14.10. *The effect of varying the consortium fraction on the observed distribution widths of constant stars.*

very strongly correlated not much of a decrease was expected in the width as a function of fraction. These plots indicate that a ratio of 1:1, i.e. giving both consortia equal weight, would yield a merged result close to optimal. This ratio would also be simpler to implement than a fraction varying as a function of magnitude. It was also decided to combine the errors using equal weights and combining them in quadrature. Due to the correlations the quoted errors of the merged data had to be analysed again and rescaled. Data originating from only one consortium did not have the errors rescaled a second time. Figure 14.11 compares the observed distribution of unit weight residuals with the probability expected for residuals with unit variance. Small discrepancies remain: there are additional wings in the observed distribution, and the central part of the distribution appears to have a slightly smaller width than expected.

A variance-weighted strategy was also considered, but rejected. The reason for this being that systematic errors probably remained which were likely to be comparable in size to the random ones, thus invalidating the premise of the weighting.

An important aspect of the merging process was the quality flagging of the transits. The basic principle behind the design of the quality flag (Field HT4 in the Hipparcos Epoch Photometry Annex) was that the lower the flag value the better the quality of the data. Thus, the higher bit settings were reserved for the more significant problems with the data. It was decided against rejecting any data at the merging stage due to the difficulty in choosing the most appropriate rejection limits. The strategy that was chosen was to flag suspected transits and keep them in the annex. Table 14.10 shows the percentage of transits that were flagged for each bit setting.

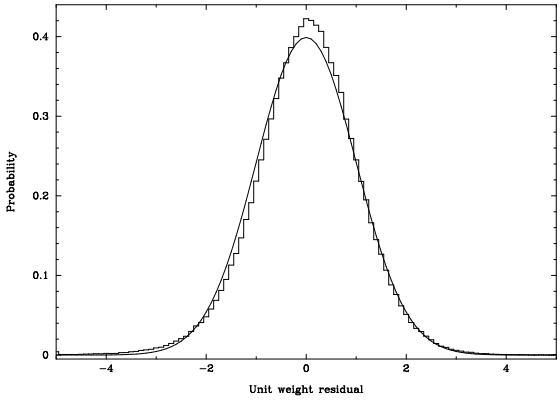

Figure 14.11. *The observed distribution of unit weight residuals for standard stars, compared with the expected probabilities for a unit variance Gaussian distribution.*

Most of the flag bit settings had various limits associated with them. The following list describes, in brief, the criteria involved in setting the bits (see Volume 1, Section 2.5):

(Bit 0) NDAC only data: no FAST data was passed to the merging process. This implies that either the transit was rejected by FAST at an earlier stage or that FAST did not process this transit;

(Bit 1) FAST only data: as above, but no NDAC transit was available to be merged;

(Bit 2) Not used;

(Bit 3) high background: the background for this transit was above 70 Hz. For faint stars there is the possibility of additional errors being present for these transits due to the uncertainty in the background estimate. The choice of the limit value is arbitrary;

(Bit 4) field of view contamination: the transit is likely to be disturbed by a star in either field of view. As described in detail in Section 14.6, the other field of view was checked against the Tycho Input Catalogue for possible contaminating stars and via the use of the difference between $Hp_{\rm dc}$ and $Hp_{\rm ac}$. Also, all transits for an entry were flagged if the Hipparcos Input Catalogue indicated that the star was a two-pointing double with a separation between 5 and 35 arcsec;

(Bit 5) FAST quality flag set: during the FAST processing if the attitude determination was classified as poor this flag was set. In NDAC such data were rejected at an earlier stage in the processing;

(Bit 6) perturbed for other identified reason: transit occurred during a period of numerous outliers. These periods were either associated with poor attitude, not identified at an earlier stage, or were close to a shutter closing event (close to Earth occultations);

(Bit 7) sun-pointing mode observation: the quality of observations taken during sun-pointing mode were believed to be affected by the non-nominal thermal environment of the satellite and were thus flagged;

(Bit 8) significant difference: if the FAST and NDAC $Hp_{\rm dc}$ values differed by more than 3σ the transit was flagged.

Table 14.10. The percentage of transits that are flagged for each bit setting in Field HT4 of the Hipparcos Epoch Photometry Annex.

Bit Setting	Percentage	Description
–	84.0	Unflagged
0	4.7	NDAC data only
1	6.3	FAST data only
2	—	Not used
3	1.7	Very high background estimate
4	3.5	Possible interfering object in either field of view
5	0.6	FAST quality flag set
6	0.2	Perturbed for other identified reason
7	1.5	Observation during sun-pointing mode
8	0.4	Significant difference between FAST and NDAC data

14.8. Properties of the Photometric Data

Measurement Errors

The average standard error per field transit in $Hp_{\rm dc}$ and $Hp_{\rm ac}$ for the merged data are given in Table 14.11. As expected, the average standard errors on $Hp_{\rm dc}$ are about half the size of those on $Hp_{\rm ac}$. Also given in this table are the average errors on the medians for stars found to be constant (stars with Field HH12 set to C). The errors on the medians are about a factor 10 smaller than the standard errors on the observations, as was expected for an average of close to 100 accepted observations per star. For the brightest stars the data are likely to be influenced by both small scale intrinsic variability and by slight inaccuracies in instrument modelling by the reduction process. Hence they do not reach the error levels one might have expected on the basis of the estimates obtained for fainter stars. In addition, the amount of integration time spent on bright stars was much shorter than on fainter stars.

The distribution of the measurement errors for individual field transit observations is shown in Figure 14.12. The widths and the wings of the distributions are primarily due to variations in the observing time (see Section 14.7). These distributions together with the data presented in Figure 14.11 clearly show that discussions concerning variability need to consider residuals weighted by their estimated error: individual observations can be of significantly different quality. This can even be the case when comparing stars of the same magnitude in different parts of the sky. The integration time spent on a star was related to the number of nearby neighbours in the Input Catalogue and photometric data for stars in more densely populated areas will be more noisy than for stars in sparsely covered areas.

Table 14.11. The average standard error per field transit and the average error on the median for stars found to be constant (stars with Field HH12 set to C).

Hp	Average transit error		Average error on median	
	dc	ac	dc	ac
2	0.0027	0.0043	0.0004	0.0008
3	0.0029	0.0049	0.0004	0.0006
4	0.0036	0.0063	0.0005	0.0008
5	0.0047	0.0091	0.0006	0.0010
6	0.0058	0.013	0.0007	0.0013
7	0.0080	0.019	0.0009	0.0019
8	0.011	0.026	0.0013	0.0027
9	0.015	0.037	0.0019	0.0039
10	0.022	0.051	0.0028	0.0055
11	0.033	0.072	0.0044	0.0079
12	0.049	0.100	0.0072	0.0107

The distribution of errors on the medians, as shown in Figure 14.13, summarizes the precision of the photometry presented in the main catalogue. For almost all these stars the precision of the median dc magnitude is of the order of 0.001 to 0.002 mag or better, while the errors on the ac magnitudes are two times larger. Figure 14.13 also shows an accumulation towards larger errors in the dc magnitudes due to variability, and in the ac magnitudes due to variability and duplicity.

An examination of the unit weight standard errors shows to what degree the corrections of the error estimates have been successful. Histograms of the observed unit weight standard errors for all stars with at least 30 observations are shown in Figure 14.14. It is clear that the situation is not ideal, and in particular for the brightest and faintest stars the variances are much influenced by reduction noise. Also clear in these diagrams are the cumulated peaks on the right-hand side of each diagram, representing the variable stars, and in some cases the presence of a companion.

Number of Observations and Distribution over Time

As described above, original observations spanned an integration time of 32/15 s. These frame transits occurred in groups of up to 9, representing together a field transit. Data have only been preserved at this level of field transits, of which over the length of the mission approximately 13 million were accumulated. These are presented in the Hipparcos Epoch Photometry Annex plus Extension. The field transits are referred to as observations.

The short-term distribution of observations was determined by the scanning speed and the configuration of the two fields of view. A series of observations therefore contains a regular pattern of: observation, 20 min gap, observation, 108 min gap, observation, 20 min gap and so on. The length of this sequence was determined by the position of the star on the scanning circle, relative to the instantaneous rotation axis of the plane of this scanning circle. Close to the rotation axis, the sequence could continue for more than a day, while perpendicular to it, the sequence would last for no more than 1 to 2

cycles. Sequences were further interrupted by perigee passages, when no observations could be made. Due to the geometry of the scanning law, the rotation axis of the plane of the scanning circle was always situated between ecliptic latitudes ±47°. Observations of stars near the ecliptic poles therefore always consist of short stretches of data, except during sun-pointing periods.

The total number of observations over the mission was also very much a function of ecliptic latitude, again resulting from the scanning law. The relations are shown in Figure 14.15. Total numbers of observations varied by a factor 10, from below 40 to 385, but the higher numbers of observations (> 200) were only found for stars close to ecliptic latitude ±47°. In the study of periodic variable stars the occurrences of data gaps are very important. Figures 14.16 and 14.17 show the distribution of the lengths of gaps and the numbers of gaps as a function of ecliptic latitudes. This distribution of data limited a reliable period search to the range 0.09 to 3 days approximately. Periods in the range 5 to 100 days were generally very poorly covered.

F. Mignard, D. Evans, F. van Leeuwen

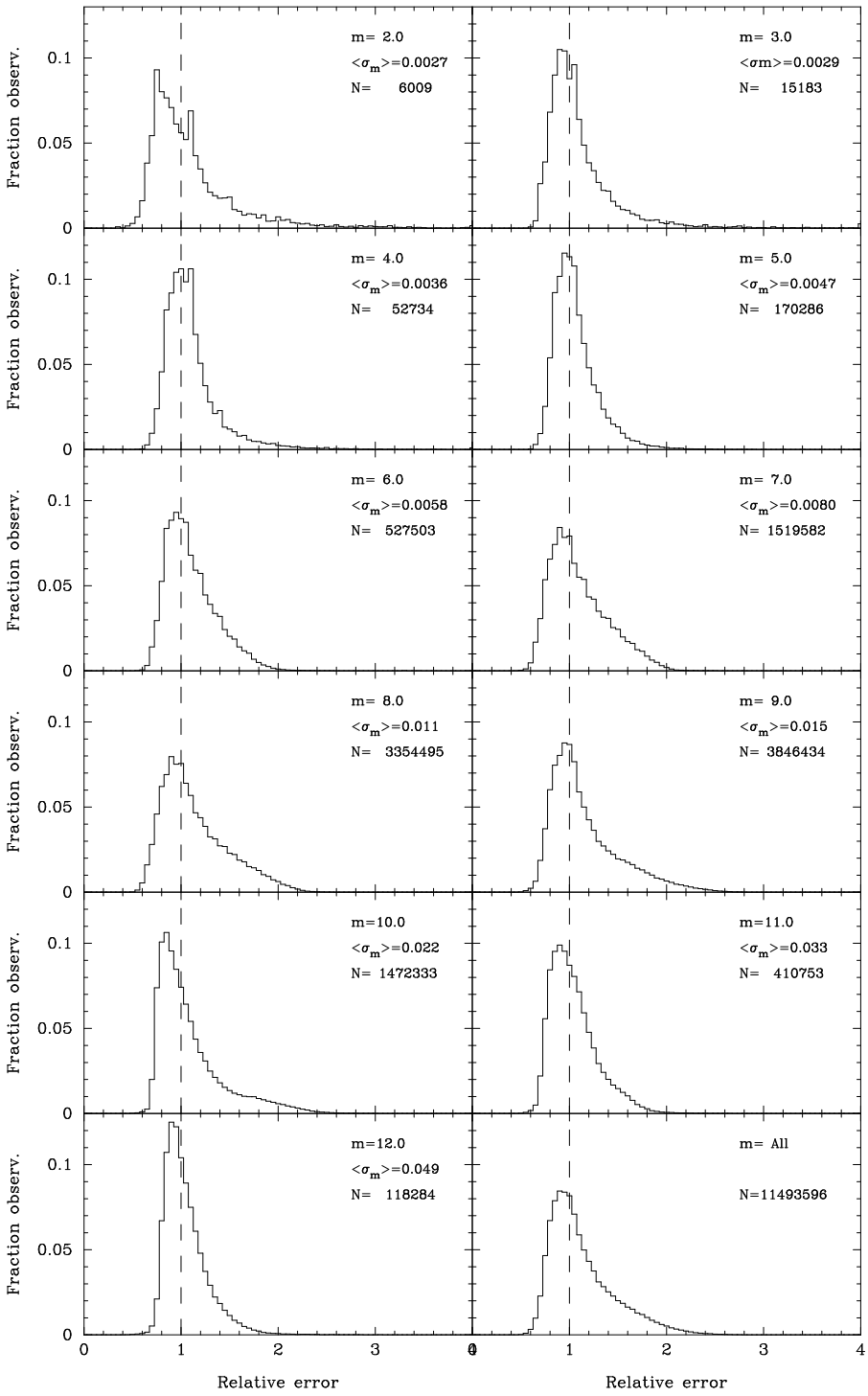

Figure 14.12. *Distribution of the measurement errors relative to the mean standard error per magnitude interval, using all measurements with error flag equal to 0. The diagram at the bottom right is the accumulated distribution of the other 11 diagrams.*

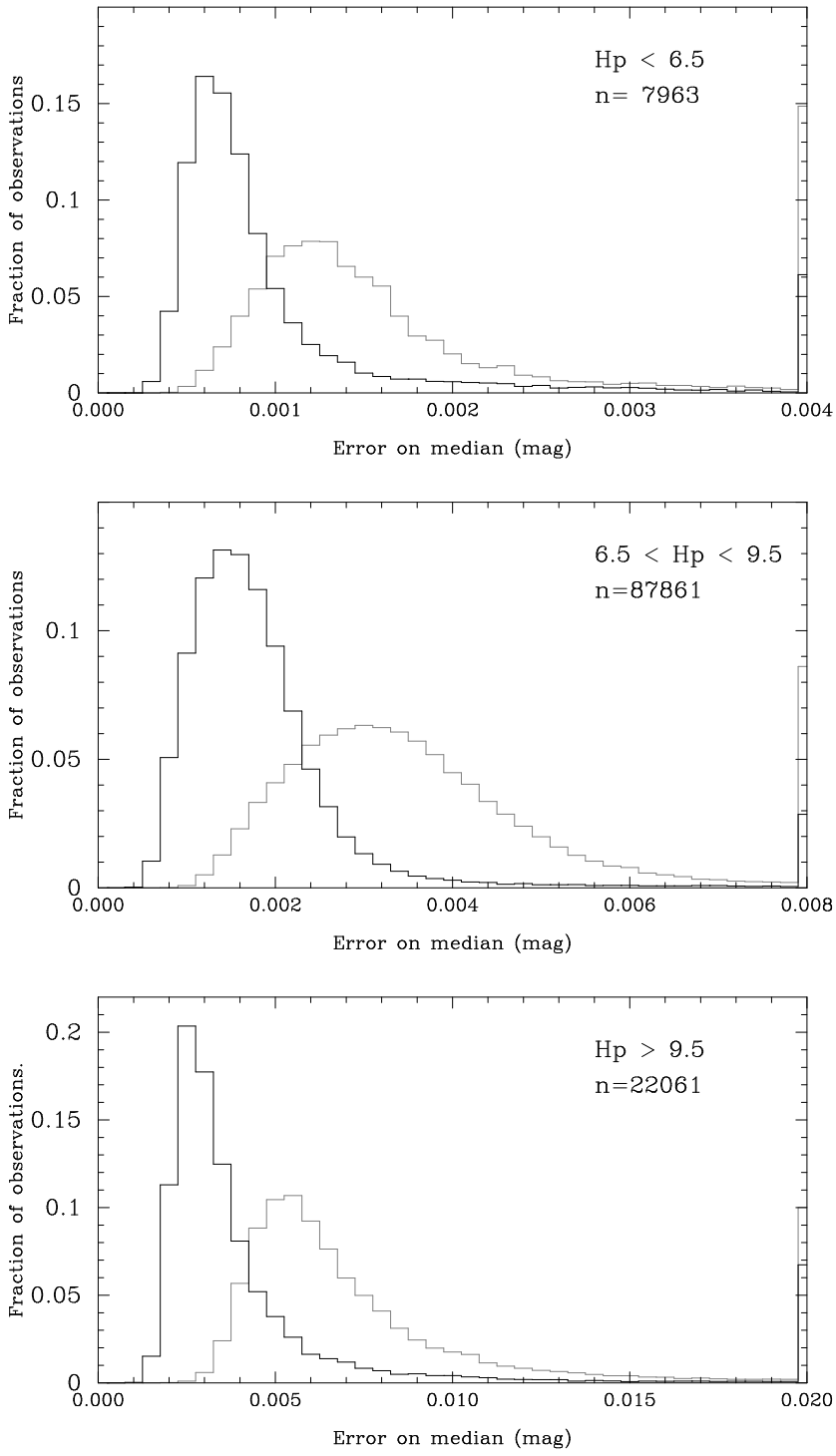

Figure 14.13. *The distribution of errors on the medians in three magnitude intervals. The distribution for the dc magnitudes is shown by the solid line, the ac magnitudes are shown by a dotted line. The accumulation on the right of each histogram represents variable stars for both ac and dc magnitudes, and in addition double stars for ac magnitudes.*

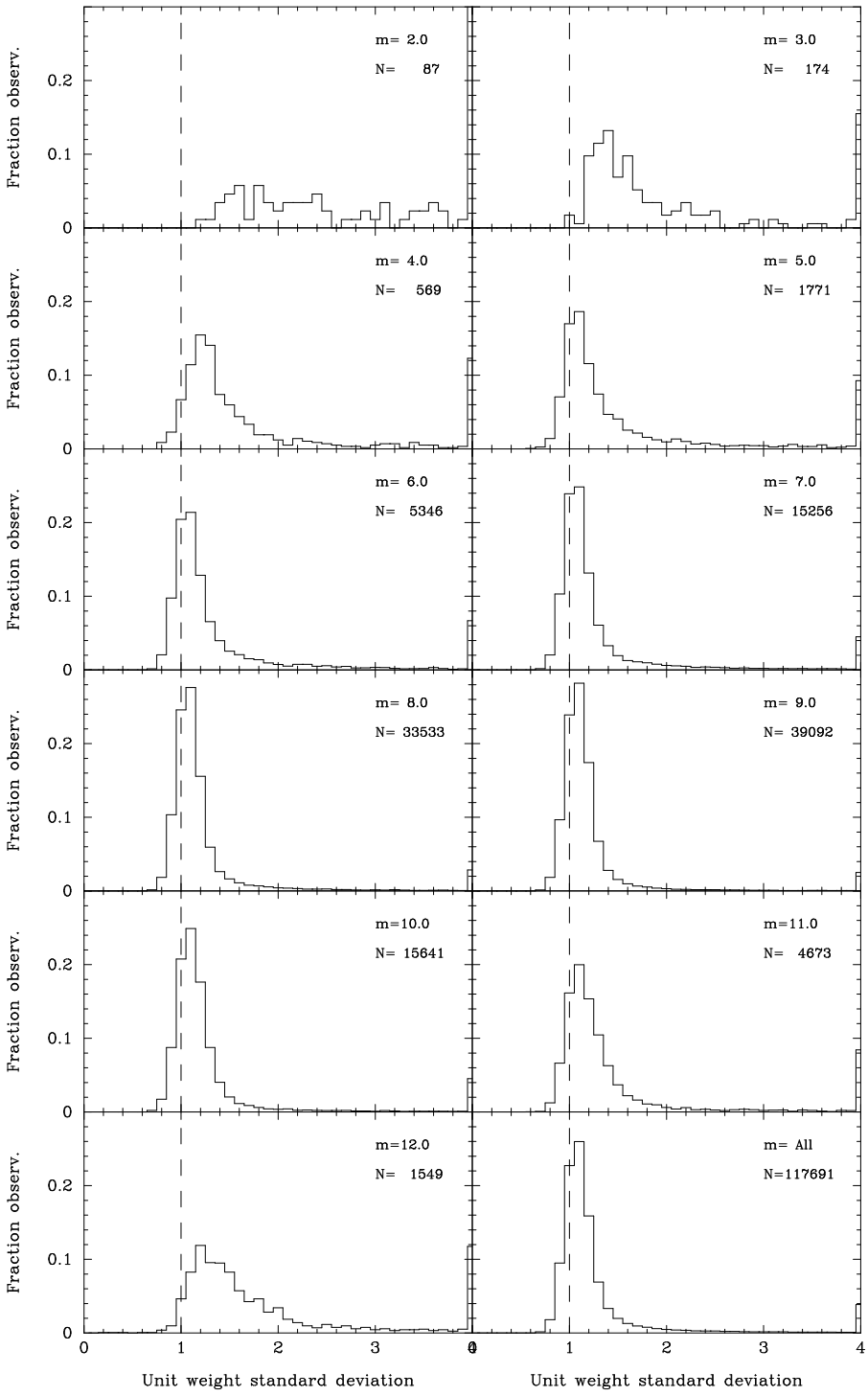

Figure 14.14. *Distribution of the unit weight standard errors. The diagram at the bottom right is the accumulated distribution of the other 11 diagrams.*

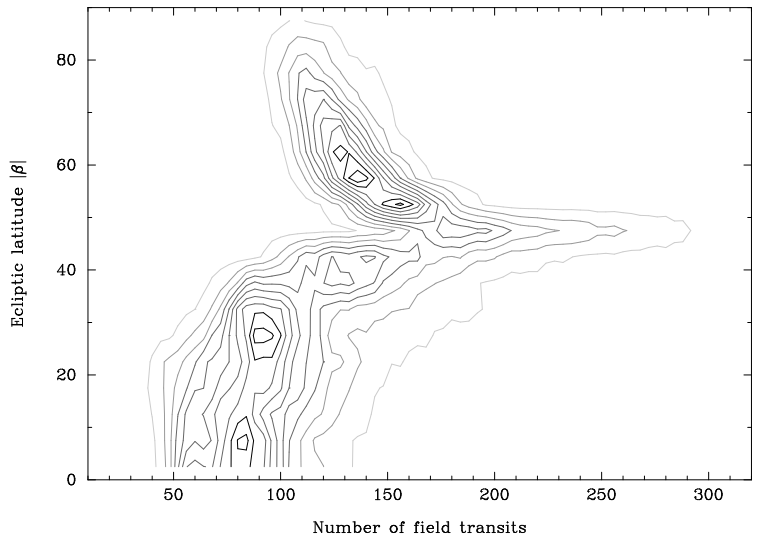

Figure 14.15. *The total number of field transits per star as function of ecliptic latitude, shown as a contour map. The first contour represents 10 stars, every next contour adds 20 stars. The highest contours represent around 200 stars. The effects of the scanning-law caused the 'discontinuity' in the distribution around 47°. The cell-size is 1 transit along the horizontal and 5° along the vertical axis.*

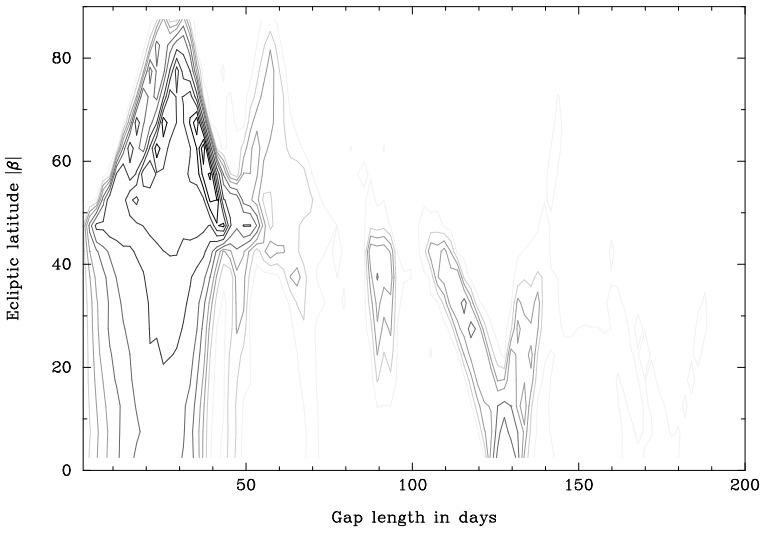

Figure 14.16. *Distributions of the lengths of gaps as a function of ecliptic latitude. Gaps longer than 1.5 days were counted for all stars observed. The feature between 50 and 60 days length was the result of gaps in the scanning due to a variety of problems with the satellite. The features for low latitudes between 85 and 140 days result directly from the scanning law. The lowest contour represents 200 gaps observed, increasing by 400 per contour until 1400, then by 600 until 2600, and then by 900 until 8900. The majority of gaps in the data are between 10 and 40 days. The cell-size is 1 day along the horizontal and 5° along the vertical axis.*

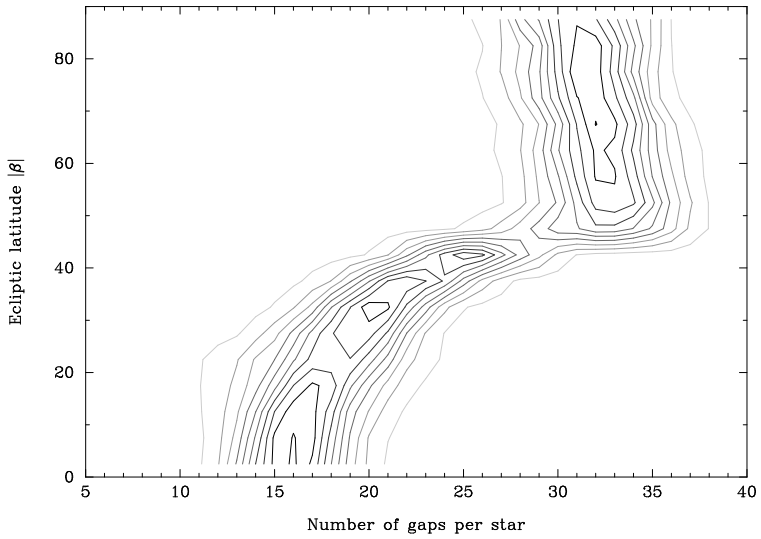

Figure 14.17. *Distributions of the number of gaps as a function of ecliptic latitude. Gaps longer than 1.5 days were counted for all stars observed. The contours follow the relative distributions of gaps. The first contour represents 1 per cent, the next 3 per cent, and every next contour a 2 per cent higher level. Thus, roughly 20 per cent of the data is found near the central ridge of the diagram, indicating that at high ecliptic latitudes the data was interrupted around 30 to 35 times, while at low ecliptic latitudes there were from 15 to 17 interruptions. The cell-size is 1 gap along the horizontal and 5° along the vertical axis.*